Article

Uncovering dynamic transcriptional regulation of methanogenesis via single-cell imaging of archaeal gene expression

Yijing Dong [1,2], Lanting Qi[1,2], Fei Zhao[1,2], Yifan Chen [3], Lewen Liang [4], Jing Wang [4], Weishu Zhao [3], Fengping Wang [3,4,5] ✉ & Heng Xu [1,2] ✉

Archaeal methanogenesis is a dynamic process regulated by various cellular and environmental signals. However, understanding this regulation is technically challenging due to the difficulty of measuring gene expression dynamics in individual archaeal cells. Here, we develop a multi-round hybridization chain reaction (HCR)-assisted single-molecule fluorescence in situ hybridization (FISH) method to quantify the transcriptional dynamics of 12 genes involved in methanogenesis in individual cells of *Methanococcoides orientis*. Under optimal growth condition, most of these genes appear to be expressed in a temporal order matching metabolic reaction order. Interestingly, an important environmental factor, Fe(III), stimulates cellular methane production without upregulating methanogenic gene expression, likely through a Fenton-reaction-triggered mechanism. Through single-cell clustering and kinetic analyses, we associate these gene expression patterns to a dynamic mixture of distinct cellular states, potentially regulated by a set of shared factors. Our work provides a quantitative framework for uncovering the mechanisms of metabolic regulation in archaea.

Cell metabolism is a complex network of biochemical reactions, each driven by specific enzymes. To fit varying environments and growth demands, cells dynamically adjust their metabolic reaction rates, primarily via transcriptional regulation of enzyme-coding genes[1–3]. Such regulation is crucial not only for guiding metabolic progress at the population level but also for creating significant cell-to-cell variability[3,4], which is essential for efficient resource utilization and population fitness in fluctuating environments[3–5]. Despite its fundamental importance, the transcriptional regulation underlying many vital metabolic pathways, particularly within the domain of archaea[6], remains elusive due to the technical challenges of monitoring multiple genes' activities in individual cells[7,8].

The unique archaeal methanogenesis pathway, which anaerobically transforms various substrates into methane (CH_4) for energy[9,10], exemplifies these challenges. This pathway is a crucial element of the global carbon cycle with significant evolutionary and ecological importance[9,11]. Previous research has outlined that it involves a conserved seven-step enzymatic reaction for CH_4 production and diverse electron transport chains (ETCs) for energy conservation[9,10]. However, the dynamic operation of this pathway, especially under critical environmental and cellular stimuli, remains poorly understood. Existing studies are limited to population-level transcriptomics measurements at specific cell growth stages[12,13], lacking the necessary precision and spatiotemporal resolution to

[1]School of Physics and Astronomy, Shanghai Jiao Tong University, Shanghai, China. [2]Institute of Natural Sciences, Shanghai Jiao Tong University, Shanghai, China. [3]State Key Laboratory of Microbial Metabolism, School of Life Sciences and Biotechnology, Shanghai Jiao Tong University, Shanghai, China. [4]Key Laboratory of Polar Ecosystem and Climate Change, Ministry of Education, and School of Oceanography, Shanghai Jiao Tong University, Shanghai, China. [5]Southern Marine Science and Engineering Guangdong Laboratory (Zhuhai), Guangdong, China. ✉e-mail: fengpingw@sjtu.edu.cn; Heng_Xu@sjtu.edu.cn

elucidate the transcriptional regulation dynamics within individual cells.

Notably, an important and prevalent environmental factor for methanogenesis is iron (Fe(III)) oxide, which could serve as a favorable electron acceptor to impact CH_4 production[14,15]. A variety of methanogen species have been observed capable of Fe(III) reduction with either inhibited or enhanced cell growth and CH_4 production, whose mechanisms are under debate[16–18]. This impact is particularly critical for methylotrophic methanogens, the dominant CH_4 producers in many marine sediments and coastal wetlands[19–21]. In these environments, methyl compounds are concentrated around the surface of highly adsorbing clay minerals, which typically contain Fe(III)[21]. However, with only geo- and biochemical measurements at the population level, the exact response of methylotrophic methanogens to Fe(III) and the underlying mechanism remain unresolved.

Answering these questions requires simultaneously quantifying the expression of multiple metabolic genes in individual archaeal cells, which has not been achieved using the standard single-cell RNA sequencing (scRNA-seq) technology[8,22]. The main challenge arises from the general difficulty of archaeal RNA extraction and the low mRNA content of archaeal cells[6,8]. The single-molecule fluorescence in situ hybridization (smFISH) technique offers a viable solution to these issues[23,24]. As an imaging-based method, smFISH has enabled precise counting and localization of mRNA molecules in individual eukaryotic and bacterial cells from intact samples without RNA extraction[24,25]. Although archaeal cell membrane consists of unique ether- and isoprene-based phospholipids, which may reduce smFISH signal[26,27], recent advances in signal amplification technologies[28–31], such as the hybridization chain reaction (HCR)[30,31], show promise for archaeal application. Besides sensitivity, imaging-based approaches are typically limited to measuring only a few genes at a time[23,31]. This limitation may be overcome by recently developed multi-round smFISH methods[4,22,32]. Consequently, multi-round HCR-assisted smFISH (smHCR-FISH) could be a potential approach for exploring methanogenic transcriptional regulation at the single-cell level.

In this study, we developed a multi-round smHCR-FISH protocol for archaea to study the transcriptional regulation of methanogenesis in a methylotrophic methanogen *Methanococcoides orientis* (type strain LMO-1) isolated from East China Sea sediment[33]. By quantifying the expression of twelve key methanogenic and ETC genes in individual cells during growth, we found specific temporal patterns of gene expression, some of which appear to align with the order of metabolic reactions. In the presence of ferrihydrite, a common source of Fe(III) in the environment, LMO-1 exhibited increased CH_4 production and oxidative stress with varied gene expression patterns, suggesting that the enzyme-independent Fenton reaction contributes to CH_4 production. Through single-cell clustering analysis, we showed that the observed gene expression patterns were due to a dynamic blend of distinct metabolic states throughout growth, whose temporal patterns varied with Fe(III) addition. Further theoretical analysis of cell-to-cell variability in mRNA levels revealed that methanogenic gene expression followed bursty transcription kinetics, whose regulation may involve several common factors. Our work demonstrates a general experimental and theoretical approach for uncovering the regulatory mechanisms in archaeal metabolism at the single-cell level.

Results

A multi-round smHCR-FISH framework for quantifying archaeal gene expression dynamics
To quantify gene expression in individual LMO-1 cells, we developed a multi-round smHCR-FISH method for archaea (Fig. 1a, see "Methods"). Quantitative imaging of archaeal mRNA has been challenging due to the unique cellular structure of archaea that affects FISH probe penetration and hybridization[6,26,30], and the low mRNA detection sensitivity of traditional smFISH[23]. To improve FISH probe penetration and

hybridization, we added a high concentration of EDTA and a blocking reagent in the hybridization buffer and optimized the permeabilizer and hybridization temperature[30,34]. And we applied HCR signal amplification to enhance the mRNA detection sensitivity[30,31] (Fig. 1a, see "Methods"). Compared to other amplification methods involving large enzyme molecules[28,29], HCR relies on an enzyme-free polymerization of short hairpin DNAs, which are easier to penetrate through complex sample structures[30,31]. To enable the detection of multiple mRNA species, we incorporated a multi-round strategy, where three mRNA species were labeled with distinct fluorophores and imaged in each round, followed by DNase I treatment to clear signals between rounds[32]. Meanwhile, we co-labeled DNA or total RNA in each round of the experiment for cell segmentation and round-to-round registration.
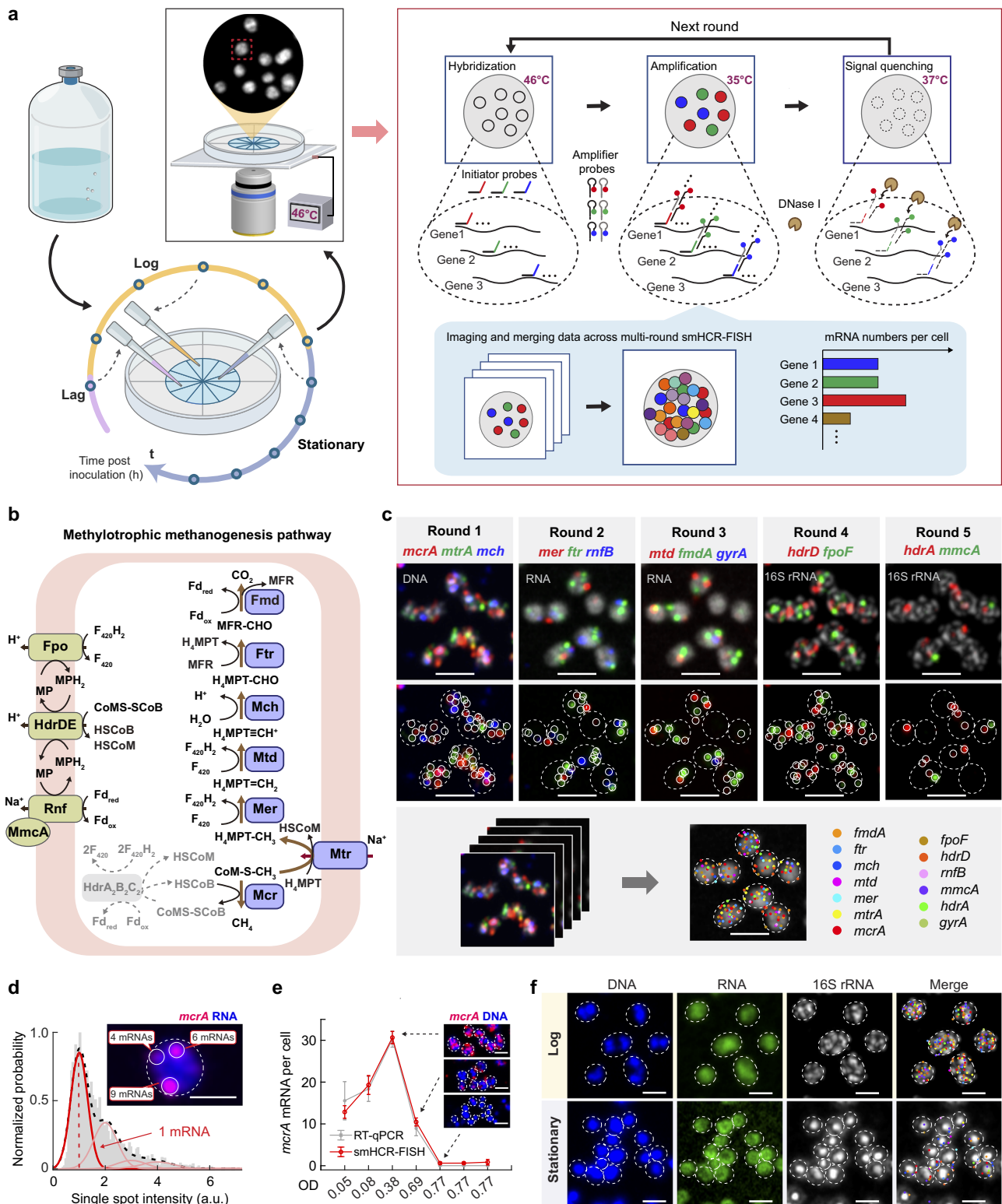
Employing this method, we imaged seven key enzyme genes in the methanogenic pathway (*fmdA, ftr, mch, mtd, mer, mtrA, mcrA*), five ETC genes (*fpoF, hdrD, rnfB, mmcA, hdrA*), as well as a housekeeping gene (*gyrA*) and 16S rRNA in individual LMO-1 cells at multiple time points across the entire growth curve (Fig. 1b, c and Supplementary Fig. 1, see Supplementary Table 1 for probe sequences). Each gene's signal appeared as numerous fluorescent spots within the cell (Fig. 1c), which represent individual or clusters of mRNA molecules. With automated identification of each gene's fluorescent spots, we individually determined the typical intensity value corresponding to a single mRNA molecule for every gene[35] (Fig. 1d). These values enabled us to estimate the number of mRNA molecules per gene in a cell (see "Methods"). Using *mcrA* as an example, we compared the cellular mRNA level derived from smHCR-FISH to that from reverse transcription-quantitative polymerase chain reaction (RT-qPCR, Fig. 1e). The quantitative agreement between the two across the growth curve corroborates the accuracy of our quantification.

Besides mRNA expression profiles, DNA and 16S rRNA signals offer valuable information about cell physiology. For example, the centralized DNA signal within the cell represents the nucleoid (Fig. 1f). In the log phase, nucleoids in many cells split into two segments, indicating chromosome duplication and cell division. The 16S rRNA signal, reflecting ribosome abundance, formed multiple clumps colocalized with mRNA signals in the log phase, indicating a coupling between transcription and translation[36,37] (Fig. 1f). In the stationary phase, this signal was concentrated in the nucleoid area, separate from mRNA signals, implying suppressed translation. Together, these results demonstrate the power of our method in elucidating single-cell activity in methanogenesis.

Temporal expressions of methanogenic and ETC genes
To understand the methanogenic growth of LMO-1, we performed measurements on cells grown under their optimal condition (without Fe(III)) over 3 days[33] (Fig. 2a–c, see "Methods"). Simultaneous monitoring of cell growth and physiology revealed that the log phase spanned from 4 h to 25 h post-inoculation (hpi), with maximal growth rate at 15 hpi (Fig. 2a). Cell size and ribosome levels roughly followed the same trend as the growth rate curve (Supplementary Fig. 2), similar to that observed in many other microbes[4,38]. During cell growth, both CH_4 production and methyl consumption increased dramatically with an overall ratio of 3:4 (Fig. 2b, c), fitting the stoichiometry of methylotrophic methanogenesis. Notably, the per-cell methyl consumption and CH_4 production rates were highest at the onset, preceding the growth rate peak, suggesting a delay in cell division during methanogenesis.

Quantifying the average expression levels of each metabolic gene at different time points revealed a trend of high expression during the log phase and low expression in the stationary phase (Fig. 2d–f and Supplementary Fig. 3). However, the specific expression pattern varied across genes, with most appearing to match the functional order of their encoded enzymes[39]. Specifically, the upstream genes, *mcrA* and *mtrA*, showed high expressions early in the log phase (peaking at ~15–20 hpi with >20 mRNAs per cell, Fig. 2e), closely aligning with the cell

the tight link between energy production and cell proliferation. Interestingly, compared to *fpoF* and *hdrD*, *rnfB* and *mmcA* exhibited significantly lower yet prolonged expression, likely due to their involvement in other metabolic processes beyond methanogenesis[10,40]. Besides the membrane-bound ETC, cytosolic HdrABC provides an alternative pathway[10]. We found that *hdrD* expression significantly exceeded *hdrA* (-15 mRNAs per cell vs. -2 mRNAs per cell, Fig. 2f), supporting the predominance of membrane-bound ETC in LMO-1's methanogenesis.

growth rate (Fig. 2a). The midstream genes, *mer*, *mtd*, and *mch*, maintained low-level expression (-5 mRNAs per cell) throughout the log phase. The very downstream genes, *ftr* and *fmdA*, were highly expressed later in the log phase (peaking at 25 hpi with -20 mRNAs per cell).

Coupled with LMO-1's methanogenesis is a putative membrane-bound ETC consisting of $F_{420}H_2$ dehydrogenase (Fpo), Na$^+$-translocating ferredoxin-NAD oxidoreductase (Rnf), and heterodisulfide reductase (HdrDE)[10,33]. Gene expression of these components all peaked at 15 hpi (Fig. 2f), synchronizing with *mcrA* and the cell growth rate, highlighting

Fig. 1 | Multi-round smHCR-FISH for archaeal gene expression. a Schematic of multi-round smHCR-FISH for labeling and imaging mRNA in archaeal cells across various growth stages. In each round, mRNAs from three genes are hybridized with primary probes, whose signals are read through the polymerization of two amplifier probes. After imaging, the targeted probes are cleared by DNase I. **b** Methylotrophic methanogenesis pathway in *Methanococcoides orientis* (LMO-1), with non-conventional pathway components in gray. Fmd, formylmethanofuran dehydrogenase; Ftr, formylmethanofuran-H4MPT formyltransferase; Mch, methenyl-H4MPT cyclohydrolase; Mtd, F420-dependent methylene H4MPT dehydrogenase; Mer, F420-dependent methylene-H4MPT reductase; Mtr, Na+-translocating methyl-H4MPT-coenzyme-M-methyltransferase; Mcr, methyl-coenzyme M reductase; Fpo, F420H2 dehydrogenase; Hdr, heterodisulfide reductase; MmcA, multi-haem C-type cytochrome; Rnf, Na+-translocating ferredoxin-NAD oxidoreductase; F420H2, reduced coenzyme F420; H4MPT, tetrahydromethanopterin; CoB, coenzyme B; CoM, coenzyme M; CoM-S-S-CoB, coenzyme B-coenzyme M heterodisulfide; Fd, ferredoxin, a two-electron carrier; red, reduced; ox, oxidized.
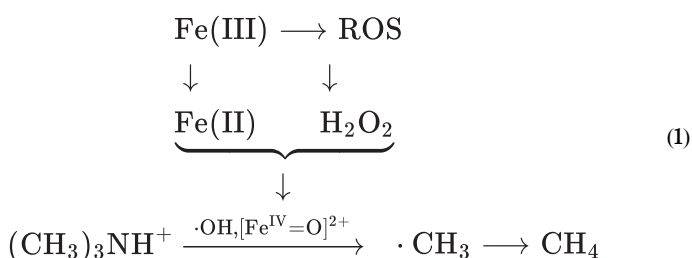
c Five-round smHCR-FISH applied to LMO-1 for labeling thirteen protein-coding genes and 16S rRNA. Top: for each round, raw fluorescence data (upper) identify mRNA spots for each gene (lower). Bottom: spots from different genes are overlaid for composite imaging. Each pseudocolor denotes a gene. Scale bars, 2 μm. **d** Intensity histogram of *mcrA* smHCR-FISH spots (4438 spots). The typical intensity corresponding to a single mRNA molecule is determined by fitting the histogram to a sum of Gaussians. Inset, smHCR-FISH image of a representative cell. Scale bar, 1 μm. A.u., arbitrary unit. **e** Average copy number of *mcrA* mRNA per cell (mean ± s.t.d.) across different growth phases measured by smHCR-FISH and RT-qPCR ($n = 3666, 6742, 6375, 7118, 6476, 4329$, and 3909 cells per time point from three biological replicates). Error bars, s.t.d. Insets, *mcrA* signals in different growth phases. Scale bars, 2 μm. **f** DNA, total RNA, and 16S rRNA signals in log- and stationary-phase cells. The 16S rRNA signal is merged with the identified mRNA spots. Each pseudocolor denotes a gene. Scale bars, 2 μm. **c**, **d**, **f** Experiments were repeated twice with similar results. Source data are provided as a Source Data file.

Fe(III) enhances CH4 production likely through Fenton chemistry

To explore the response of LMO-1 cells towards Fe(III), we examined cells grown in cultures amended with ferrihydrite, a common iron oxide mineral in the environment (Fig. 3a–d and Supplementary Fig. 4a, b, see "Methods"). Although the duration of the log phase remained unchanged, the early-stage growth of LMO-1 cells was markedly retarded, with the peak rate occurring at 20 hpi (Fig. 3a). This coincided with increased cell size and decreased ribosome levels (Supplementary Fig. 4a, b), suggesting oxidative stress[41,42]. Further measuring cellular reactive oxygen species (ROS) and the expression of an oxidative stress response gene, *katG* (catalase/peroxidase HPI), both showed significant increase under ferrihydrite amendment (Fig. 3e, f, see "Methods"), confirming Fe(III)-induced oxidative stress. During cell growth, we observed continuous Fe(II) production, peaking at 9–15 hpi (Fig. 3b and Supplementary Fig. 4c–e), indicating LMO-1's Fe(III) reduction capability. Meanwhile, methyl consumption and CH4 production escalated, with significantly increased peak rates at 15 hpi (Fig. 3c, d), indicating that Fe(III) enhances CH4 production.

To understand the mechanism of such enhancement, we analyzed the expression of methanogenic and ETC genes under ferrihydrite treatment (Fig. 3g–i and Supplementary Fig. 5a, b). Compared to the optimal growth condition, many genes exhibited decreased or delayed expression. Specifically, *mcrA* and *mtrA* expressions peaked markedly later at 26 hpi, while *mtd, mch, ftr, fmdA*, and all membrane-bound ETC genes showed a significant decline in expression (Fig. 3h, i). These changes could be partly attributed to biofilm formation on the mineral surface (Fig. 3g), which increased energy consumption and impeded substrate diffusion, adversely impacting cell growth and metabolism[43,44]. However, the similarity in gene expression levels between mineral-associated and planktonic cells suggests that biofilm formation had limited impact (Supplementary Fig. 5c). Nevertheless, the drop and delay in gene expression are inconsistent with the observed increase in CH4 production, suggesting the presence of a faster enzyme-independent CH4 production mechanism under iron exposure.

One potential mechanism is through the Fenton reaction, which was reported to drive CH4 formation in non-methanogenic organisms[45,46], i.e.,

$$\text{Fe(III)} \longrightarrow \text{ROS}$$
$$\downarrow \qquad \downarrow$$
$$\underbrace{\text{Fe(II)} \qquad \text{H}_2\text{O}_2} \tag{1}$$
$$\downarrow$$
$$(\text{CH}_3)_3\text{NH}^+ \xrightarrow{\cdot\text{OH},[\text{Fe}^{IV}=\text{O}]^{2+}} \cdot\text{CH}_3 \longrightarrow \text{CH}_4$$

With Fe(III)-induced ROS (particularly H2O2) and Fe(II) reduced from Fe(III) (Fig. 3j, k), the reaction generates ·OH radicals and $[\text{Fe}^{IV} = \text{O}]^{2+}$ complexes, both of which drive the conversion of methylated compounds into methyl radicals and, subsequently, CH4. To test the possibility of this mechanism, we measured the stable carbon isotope fractionation ($\delta^{13}C$) of the produced CH4 (Fig. 3j, see "Methods"), which serves as a fingerprint for the underlying biochemical processes[45,47]. The $\delta^{13}C$ value from Fe(III)-amended condition was less negative (−83 ± 3.8‰) compared to that from the optimal condition (−95 ± 0.4‰), while closer to the $\delta^{13}C$ signature of abiotic Fenton reaction (−43.7 ± 0.05‰). This suggests a Fenton-based mechanism for CH4 production in Fe(III)-amended LMO-1. Moreover, we found that CH4 production was substantially faster in Fe(III)-amended cell culture than in abiotic reactions (Fig. 3k, see "Methods"), suggesting that such Fenton-based mechanism occurs predominantly within the cell.

Notably, while the Fenton reaction may facilitate CH4 production, it does not contribute to ATP synthesis for the cell. Hence, the remaining gene expressions are essential for cell growth. Interestingly, *mer* and *ftr* showed nearly identical expression trends (Fig. 3h), revealing iron-induced coupling. Moreover, unlike membrane-bound ETC genes, *hdrA* was overexpressed in the mid-late log phase (10–26 hpi), implying a shift towards the cytosolic HdrABC-based ETC over the HdrDE-based system (Fig. 3i). This transition aligns with previous speculation that Fe(III) reduction may occur through Rnf/MmcA-mediated oxidation of ferredoxin, disrupting the HdrDE-based ETC to induce cellular ROS, whose rebalance requires HdrABC-based electron bifurcation[16,48]. Together, these observations suggest a coupling mechanism between Fe(III) reduction and Fenton-based CH4 production in methylotrophic methanogens.

Single-cell profiling indicates dynamic metabolic heterogeneity in methanogenesis

Beyond individual gene expression, different genes' activities may be coordinated within a single cell, leading to metabolic heterogeneity[3,4]. To examine this effect in methanogenesis, we performed uniform manifold approximation and projection (UMAP) dimensionality reduction and clustering analysis on single-cell gene expression data (Fig. 4a, b, Supplementary Figs. 6, 7, see "Methods")[4,49]. Analyzing all time points together, we identified multiple subgroups of cells, each with a unique gene expression profile and temporal pattern (Fig. 4a–d). Intriguingly, the seemingly well-mixed cell culture comprised multiple subgroups at any given time.

In the optimal growth condition, LMO-1 cells in the log phase were categorized into four main subgroups (Groups 1–4) that dominated successively (Fig. 4a, c). Group 1, primarily appearing in the early log phase (4–9 hpi), was marked by active *mcrA*, *mtrA*, and *mch*. Groups 2 and 3, prevalent in the early-mid log phase (4–15 hpi), showed widespread activation of methanogenic/ETC genes, consistent with
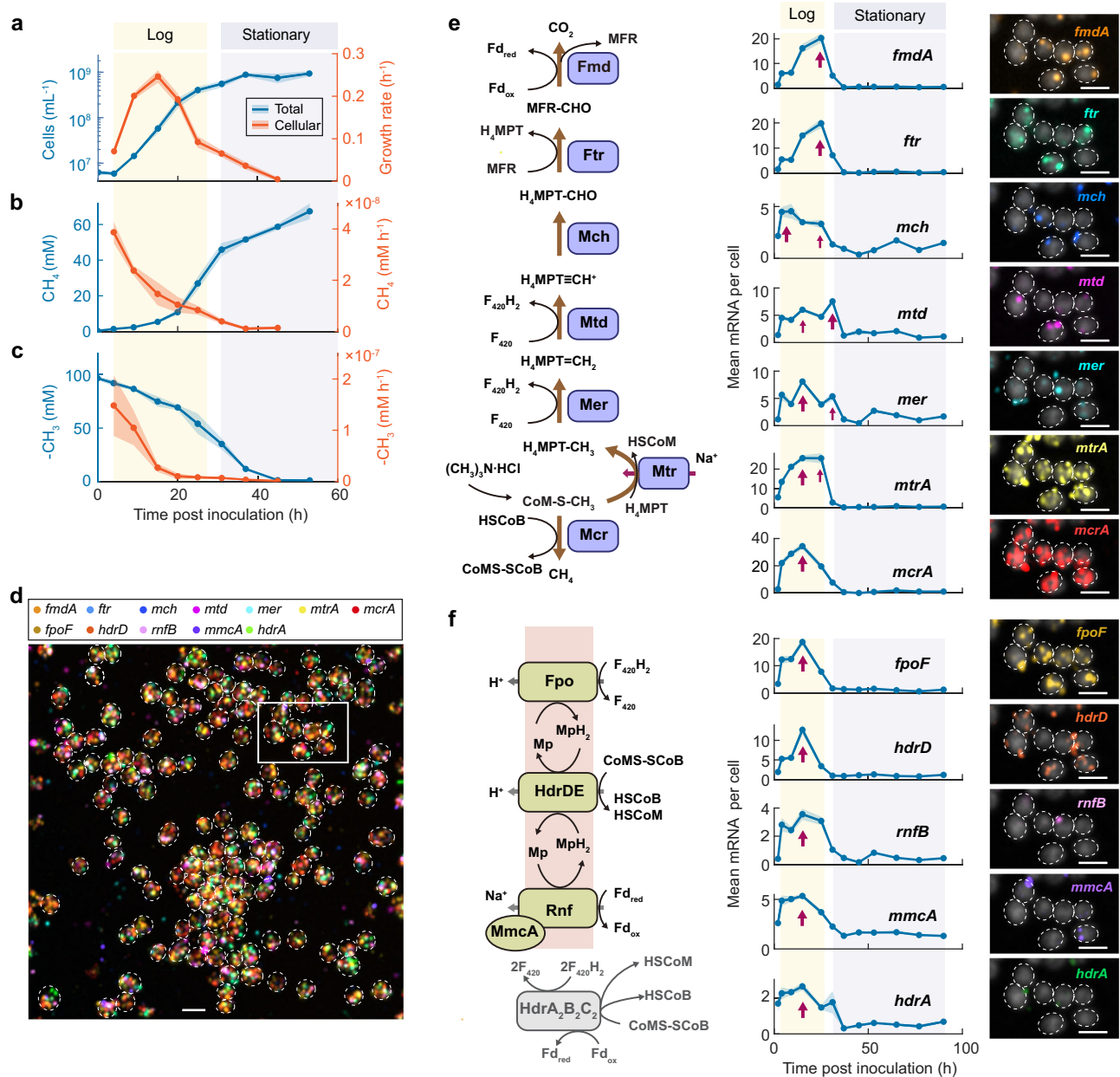
Fig. 2 | Methanogenic and ETC gene expression patterns match their functional order. a–c Cumulative (blue) and rate (red) curves (mean ± s.e.m.) for cell growth (**a**), CH₄ production (**b**), and methyl consumption (**c**) over time under the optimal growth condition, respectively. Data from three biological replicates. Shadings indicate s.e.m. **d** Representative image of LMO-1 cells grown in the optimal condition (15 hpi), with seven methanogenic enzyme genes and five ETC genes labeled, each represented by a unique color. Scale bar, 2 μm. Experiments were repeated twice with similar results. **e**, **f** Temporal expression patterns (mean ± s.e.m.) of methanogenic genes (**e**) and ETC genes (**f**), respectively. Left: simplified pathway diagrams, with inactive components in gray. Middle: For each gene, mRNA level (y-axis) is plotted as a function of time. Red arrows indicate expression peaks. Log-phase data were from two biological replicates with ≥10 fields of view (FOVs). Shadings indicate s.e.m. calculated from the means of each field of view. n = 8787, 15,150, 14,001, 15,835, 23,096, 4707, 5346, 2568, 3575, 3017, 3009, and 3054 cells at time points from early to late. Right: smHCR-FISH signals for each gene, corresponding to the white box in (**d**). Scale bars, 2 μm. Source data are provided as a Source Data file.

methanogenic and cell growth peaks. In the late log phase (15–25 hpi), Group 4 with inactive *hdrA* became dominant, revealing the preference for HdrDE-based ETC. At the transition to the stationary phase (31 hpi), Group 5 emerged briefly with active *mcrA* and *ftr*, marking the cessation of methanogenic cell growth (Fig. 4a, c). Upon entering the stationary phase, multiple subgroups (Groups 6–16) arose, each with limited methanogenic/ETC genes expressing (Fig. 4a, c), suggesting a strategic shift to leverage residual metabolic products using proteins translated in previous stages.

With Fe(III) addition, cells formed distinct subgroups, some corresponding to those in the optimal growth condition but with shifted timing (Fig. 4b, d). For example, Groups 1′–4′, which dominated sequentially through the log phase, inversely corresponded to Groups 1–4 in the optimal growth condition, reflecting the Fe(III)-induced rearrangement of gene expression (Fig. 3h, i). Like in the optimal growth condition, stationary-phase subgroups (Groups 5′–13′) showed limited gene expression, suggesting a conserved strategy for utilizing metabolic leftovers.
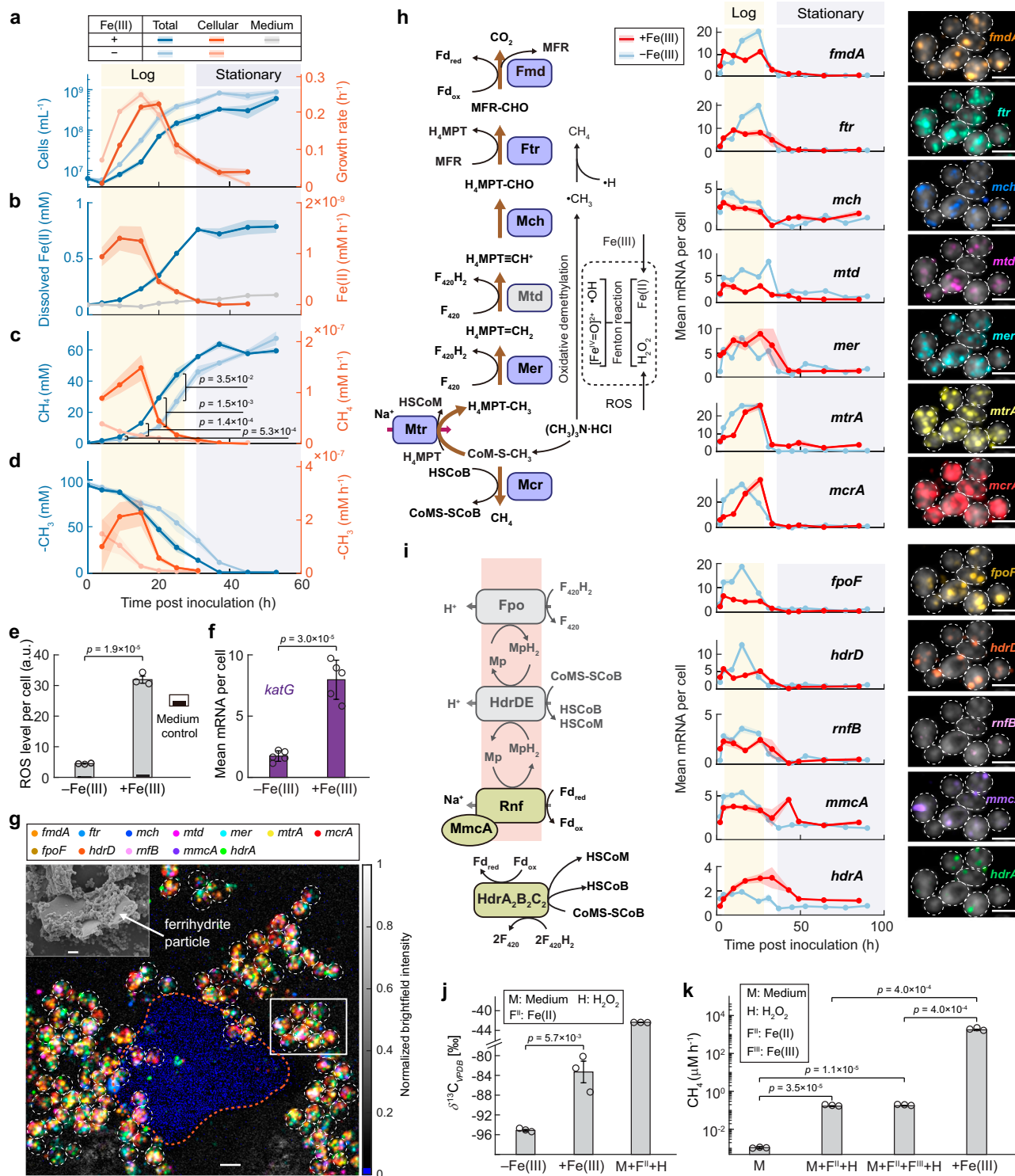
## Multiple regulatory factors drive bursty methanogenic gene expression

To understand the mechanism of dynamic gene expression profiles, we analyzed cell-to-cell variability in each gene's expression, which reflects the microscopic, stochastic transcription kinetics[50,51]. A simple metric for this variability is the Fano Factor (F, variance-to-mean ratio) of mRNA copy number per cell. $F \approx 1$ implies consistent mRNA production, whereas $F > 1$ indicates bursty production[51,52]. Our analysis revealed that, except for the housekeeping gene *gyrA*, all methanogenic and ETC genes in LMO-1 appeared to exhibit bursty transcription

in both optimal and ferrihydrite-amended conditions (Fig. 5a), akin to that in bacteria and eukaryotes[50,52].

We then applied a simple theoretical model to infer detailed transcription kinetics from the single-cell mRNA copy number distribution for each gene over time (Fig. 5b, Supplementary Figs. 8, 9, see "Methods"). In this model, the gene stochastically switches between an active ("on") and an inactive ("off") state, with mRNAs produced solely in the active state, followed by random degradation (Fig. 5c)[50,51]. Gene activation and inactivation, mRNA synthesis, and degradation are characterized by Poissonian rates k_{ON}, k_{OFF}, k_{TX},

Fig. 3 | Fe(III) amendment enhances CH₄ production with rearranged gene expression. a–d Cumulative (blue) and rate (red) curves (mean ± s.e.m.) for cell growth (**a**), Fe(II) production (**b**), CH₄ production (**c**), and methyl consumption (**d**) over time under optimal (−Fe(III), dim color) and ferrihydrite-amended (+Fe(III), bright color) conditions, respectively. The gray line in (**b**) represents the background Fe(II) level in the ferrihydrite-amended medium without biomass. Shadings indicate s.e.m. **e, f** Cellular ROS level (**e**, mean ± s.e.m.) and *katG* expression level (**f**, mean ± s.e.m.) under optimal (−Fe(III)) and ferrihydrite-amended (+Fe(III)) conditions (17 hpi). a.u. arbitrary unit. **g** Representative image of LMO-1 cells grown in ferrihydrite-amended condition (17 hpi), with seven methanogenic enzyme genes and five ETC genes labeled, each represented by a unique color. The background signal is the brightfield image. Scale bar, 2 μm. Inset, ferrihydrite mineral particle observed under scanning electron microscopy (SEM). Scale bar, 2 μm. Experiments were repeated twice with similar results. **h, i** Temporal expression patterns (mean ± s.e.m.) of methanogenic genes (**h**) and ETC genes (**i**), respectively. Left: simplified pathway diagrams involving the Fenton reaction, with inactive components in gray. Middle: For each gene, mRNA levels (*y*-axis) with (*n* = 953,

3953, 7205, 7219, 9794, 255, 468, 1545, 953, and 904 cells at time points from early to late) and without (*n* = 8787, 15,150, 14,001, 15,835, 23,096, 4707, 5346, 2568, 3575, 3017, 3009, and 3054 cells at time points from early to late) Fe(III) addition are plotted as a function of time, respectively. Log-phase data were from two biological replicates with ≥5 FOVs. Shadings indicate s.e.m. calculated from the means of each field of view. Right: smHCR-FISH signals for each gene, corresponding to the white box in (**g**). Scale bars, 2 μm. **j** Stable carbon isotope values (mean ± s.e.m.) of CH₄ production under optimal (−Fe(III)) and ferrihydrite-amended (+Fe(III)) conditions (31 hpi). **k** Abiotic CH₄ production rate (mean ± s.e.m.) in cell-free culture media amended with Fe(II) and H₂O₂, with bare culture medium and Fe(III)-amended cell culture serving as negative and positive controls, respectively. **a–e, j, k** Data from three biological replicates. **f** For each growth condition, cells are from two biological replicates with five FOVs. *n* = 3879 and 1412 cells for optimal (−Fe(III)) and ferrihydrite-amended (+Fe(III)) conditions, respectively. S.e.m., calculated from the means of each field of view. **c, e, f, j, k** Statistical analysis was performed using two-sided *t*-test. Source data are provided as a Source Data file.
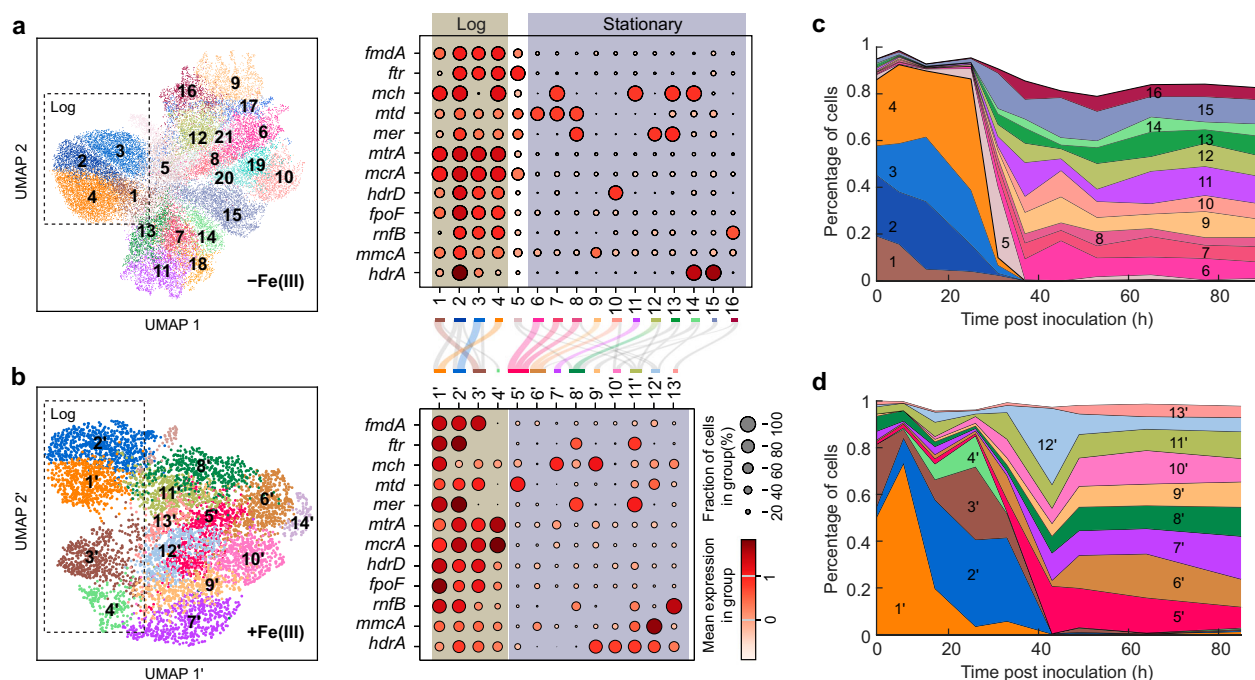
Fig. 4 | Single-cell analysis reveals dynamic clusters of methanogenic/ETC gene expression. a, b UMAP analysis of methanogenic and ETC gene expression from all time points under optimal (−Fe(III), **a**) and ferrihydrite-amended (+Fe(III), **b**) conditions. Each dot represents a single cell. Identified clusters are shown in different colors, with a Sankey diagram relating clusters in two growth conditions. Each cluster's gene expression profile is displayed on the right. **c, d** Cell distribution in each cluster as a function of time for optimal (−Fe(III), **c**) and ferrihydrite-amended (+Fe(III), **d**) conditions. **a, c** *n* = 32,885 cells from 11 time points. **b, d** *n* = 6408 cells from nine time points. Source data are provided as a Source Data file.

and k_D, respectively. By comparing model predictions with experimental data, we estimated kinetic parameters for each gene, which revealed that transcriptional regulation in methanogenesis primarily modulates k_{ON} and k_{OFF}, with k_{TX} and k_D remaining constant (Fig. 5d, e, Supplementary Fig. 10a).

To further understand the regulatory relationships among genes, we compared the temporal patterns of k_{ON} and k_{OFF} (in its reciprocal form), which are signatures of the corresponding regulators, across different genes (Supplementary Fig. 10a–e, see "Methods"). Notably, the temporal patterns of these kinetic parameters during the log phase fall into distinct categories (Fig. 5f, g), suggesting the involvement of distinct regulatory factors. Specifically, in the optimal growth condition (Fig. 5d, f), the k_{ON} for *mcrA*, *mtrA*, *mch*, and *fmdA* displayed a sigmoidal decline over time, similar to the methyl concentration curve (Fig. 2d), suggesting

methyl-containing reactants or intermediates as potential activators for these genes[46]. Similarly, the k_{ON} for *ftr*, *rnfB*, and *fpoF*, and the $1/k_{OFF}$ for *mcrA* showed a pulsing pattern aligning with the growth rate curve (Fig. 2a), suggesting factors related to cell proliferation, like intracellular ATP level, as potential regulators. Further similarities revealed in this analysis suggest other regulatory factors, whose identities are yet to be uncovered.

Compared to the optimal growth condition, Fe(III) addition significantly altered regulatory relationships among genes (Fig. 5e, g). Intriguingly, the k_{ON} for *mcrA*, *mtrA*, *mch*, and *fmdA*, which are potentially activated by methyl-containing compounds, declined more rapidly than under the optimal condition, consistent with the accelerated methyl consumption due to the Fenton reaction. During the log phase, both the k_{ON}- and k_{OFF}-regulations of *ftr* and *mer* were tightly coupled, while the k_{ON} of *fpoF* and *rnfB* shifted their regulatory
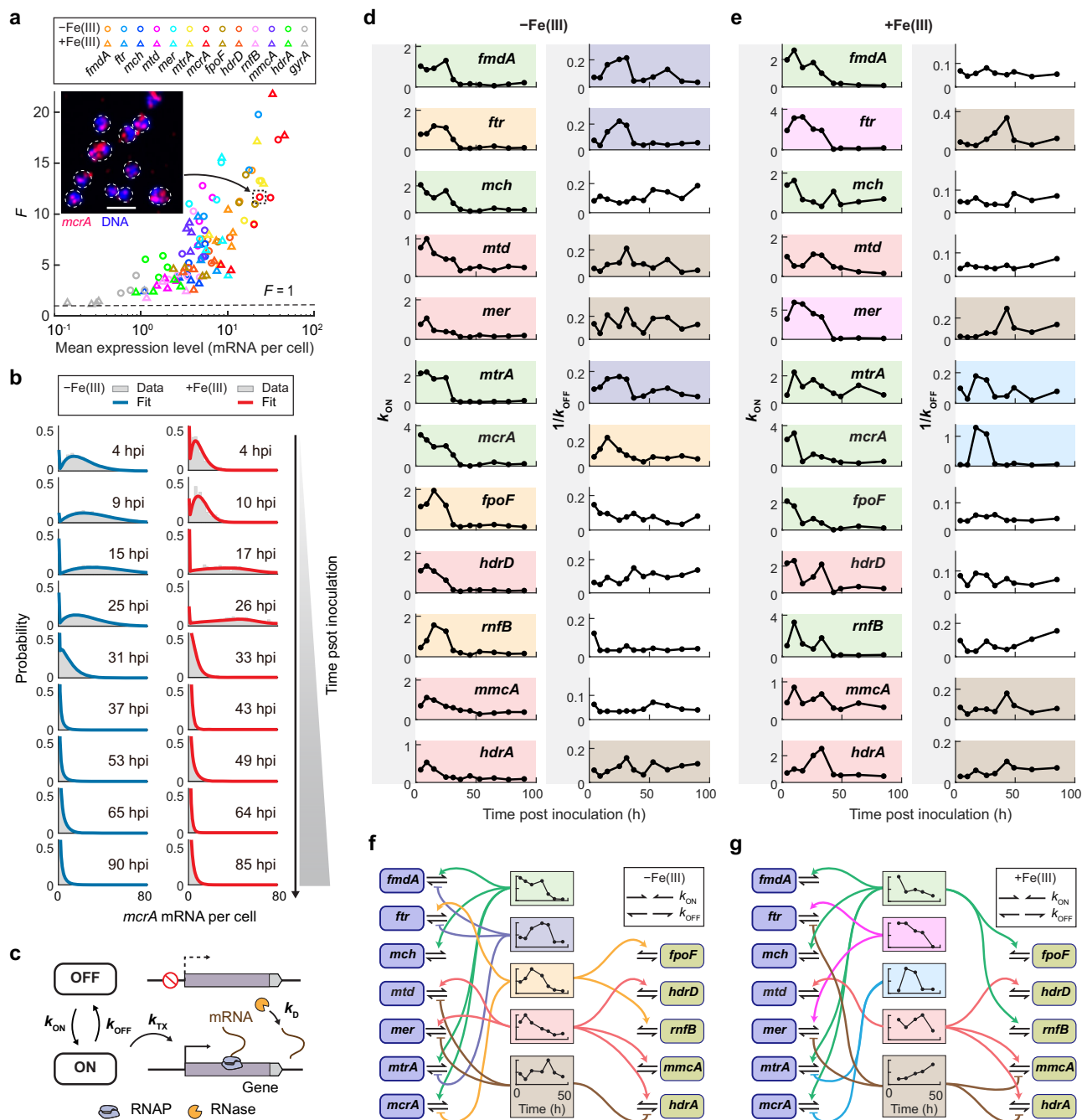
Fig. 5 | Kinetic modeling reveals the transcriptional regulation mechanism of methanogenesis. a Fano factor as a function of the mean expression level for seven methanogenic enzyme genes, five ETC genes, and a housekeeping gene under optimal (−Fe(III), circles, $n = 7609$ cells) and ferrihydrite-amended (+Fe(III), triangles, $n = 2283$ cells) conditions. Each gene is represented by a unique color. Solid line, theoretical prediction for consistent mRNA production. Inset, cell-to-cell variability in *mcrA* signals. Scale bar, 2 µm. b Histograms of *mcrA* mRNA copy number per cell at various growth stages under optimal (−Fe(III), left, $n = 1357, 625,$ 2862, 2765, 4707, 5346, 3575, 3017, and 3054 cells at time points from early to late) and ferrihydrite-amended (+Fe(III), right, $n = 315, 304, 678, 986, 255, 468, 1545, 953,$ and 904 cells at time points from early to late) conditions. The experimental data (gray bars) were fitted to a two-state model (solid lines). c Schematic of the two-

state transcription model with stochastic ON/OFF switching, mRNA synthesis, and degradation. d, e Temporal patterns of k_{ON} and $1/k_{OFF}$, in units of k_D and $1/k_D$, for different genes under optimal (−Fe(III), d, k values estimated from $n = 1357, 625,$ 2862, 2765, 4707, 5346, 2568, 3575, 3017, 3009, and 3054 cells for each time point) and ferrihydrite-amended (+Fe(III), e, k values estimated from $n = 315, 304, 678,$ 986, 255, 468, 1545, 953, and 904 cells for each time point) conditions. Background shadings indicate pattern groups. f, g Conceptual diagrams of methanogenic transcriptional regulation under optimal (−Fe(III), f) and ferrihydrite-amended (+Fe(III), g) conditions. k_{ON} and $1/k_{OFF}$ for different genes are regulated by multiple factors. Fe(III) addition significantly modifies the regulatory scheme. Source data are provided as a Source Data file.

affiliations from the $1/k_{OFF}$ to the k_{ON} of *mcrA*. Moreover, although the k_{ON} of *hdrD* and *hdrA* remained coupled, *hdrA*'s peak activation rate surged by >4-fold, accounting for the upregulation of *hdrA* (Fig. 3i). Conversely, the $1/k_{OFF}$ of *mtd, mch, fmdA*, and all membrane-bound

ETC genes diminished, agreeing with the reduction in their expression level (Fig. 3h, i). These modifications, potentially driven by ROS, elucidate the transcriptional regulation mechanism of Fe(III)-enhanced methanogenesis.

Discussion

So far, studies of archaeal metabolic dynamics have been restricted to population-level measurements, primarily via RNA-seq, due to the unique cellular structure and low mRNA content of archaeal cells[7,8,26,27]. However, biases in transcript quantification and cellular normalization across samples prevent these approaches from accurately reconstructing the dynamics of metabolic gene activities[53]. Our multi-round smHCR-FISH approach, specifically improved for archaea, offers a solution to this challenge. Using methanogenesis in LMO-1 as an example, we demonstrated the power of this method in uncovering the intricate transcriptional regulation mechanisms of a critical archaeal metabolism at the single-cell level.

In both eukaryotes and bacteria, metabolic genes have been shown to express in specific temporal orders that typically match metabolic reaction progress and cell physiology demands[3,4,54]. This "just-when-need" strategy of gene expression is critical to cell survival and may be used to verify metabolic reaction orders proposed from biochemical or genomic analyses[39]. Our findings suggest that this strategy may apply also to archaeal metabolism. The observed time difference between the expression of upstream and downstream genes and the asynchrony between methyl consumption and the production of CH_4 and CO_2 help understand the slow dynamics of methanogenesis. Besides this strategy, differential tuning of each enzyme's half-life time may be an additional strategy for optimizing the working duration of each methanogenic step[55,56], whose effect is yet to be determined. Further examining gene expression and protein life-cycle patterns in more metabolic pathways will help uncover the general mechanisms and design principles of archaeal metabolism, which are essential for environmental protection and high-value compound production.

Previous biochemical studies suggest that Fe(III) reduction, with its higher free energy yield, inhibits the growth and CH_4 production of methanogens[17,18]. Although this phenomenon was observed in hydrogenotrophic methanogens[18], it appears contradictory to geochemical findings of overlapping methanogenesis and Fe(III) reduction[14,15,21]. On the other hand, acetotrophic methanogens with Fe(III) amendment have shown enhanced CH_4 production and cell growth, consistent with geochemical findings[14,16]. However, without single-cell gene expression data, the mechanism of this phenomenon remains debated[16]. Our studies showed a yet different response of methylotrophic methanogens to Fe(III), with inhibited cell growth and enhanced CH_4 production, highlighting the diversity of methanogens' survival strategies under environmental challenges.

Particularly, our single-cell measurements suggest that LMO-1's response to Fe(III) may involve an iron-dependent, enzyme-free CH_4 production mechanism, likely through the Fenton reaction. This mechanism has been observed in various non-methanogenic organisms, such as plants, fungi, algae, and bacteria[45]. Our findings provide evidence of its existence in methanogens, where abiological CH_4 production has been overlooked. However, its functioning and integration with the biochemical methanogenesis pathway may vary among species and environments. For example, the observed inhibition of hydrogenotrophic methanogenesis under Fe(III) amendment could be due to a lack of methyl substrates needed for the Fenton reaction[17,18]. Moreover, since methanogenesis is a relic of ancient anaerobic metabolism[9], the existence of this ROS-consuming CH_4 production mechanism suggests its early evolutionary development as a partial remedy to oxidative stress[45,57].

Besides bulk-level dynamics, LMO-1 gene expression exhibited significant cell-to-cell variability, leading to diverse metabolic states. By analyzing single-cell mRNA statistics, we showed that such heterogeneity stems from bursty transcription of archaeal genes–a behavior previously observed in eukaryotes and bacteria[52]. Our findings indicate that, despite distinct transcriptional machinery[58], gene transcription across all three domains of life may follow a unified two-state kinetics[52]. However, the regulation of such kinetics seems to be domain-specific. Bacterial transcriptional regulation primarily alters k_{OFF}, while eukaryotic regulation may adjust both k_{ON} and k_{OFF}[50,52]. Intriguingly, archaeal transcriptional regulation is kinetically closer to the eukaryotic one, consistent with the evolutionary connection between these two domains.

Following transcription kinetics analysis, a further challenge is to pinpoint the underlying regulatory factors for the gene network[59,60]. Typical approaches like genomic analysis and genetic/biochemical validations can be labor-intensive and less suitable for non-model organisms[13]. In this paper, we developed a method to infer common regulators in methanogenesis by comparing the temporal patterns of k_{ON} and k_{OFF} across different genes. The predicted regulatory relationships align with previous bioinformatics predictions for hydrogenotrophic methanogens[13] and provide additional insights, offering broader applications for studying other metabolic gene networks.

Our multi-round smHCR-FISH method facilitates high-throughput, quantitative single-cell analysis of archaeal gene expression. With adaptation to higher background fluorescence, the approach can be applied to complex natural microbial communities (Supplementary Fig. 11), where archaeal and bacterial metabolisms are interlinked[6,7,61]. Further integrating this method with microfluidics and alternative probe removal techniques[22], and combining it with immunostaining and metabolomics will yield a deeper understanding of archaeal metabolic regulation[62,63].

Methods

Cell cultivation

Methanococcoides orientis strain LMO-1 isolated from East China Sea sediment (30°48′34.32″ N, 122°48′56.76″ E) was cultured anaerobically in the dark in a modified DSM medium 141c with 30 mM trimethylamine hydrochloride (substrate for methanogenesis) and a nitrogen-filling headspace ($V_{gas}/V_{liquid} \approx 1{:}1$)[33]. For Fe(III) amendment, 10 mM ferrihydrite was added to the culture medium following a standard recipe[64]. For biochemical assays, cells were inoculated at 5% in 10 mL of freshly prepared medium and incubated in 20 mL headspace vials at 35 °C. Three replicates were prepared for each time point. For smHCR-FISH experiments, 80 mL of cell culture (5% inoculation) was prepared in 150 mL serum bottles at 35 °C. At each designated time point, 3 mL of culture was sampled, fixed with 1 mL of 8% (v/v) paraformaldehyde for 12 h at 4 °C, washed twice with 1× PBS (10 min each), and stored in a 1:1 (v/v) mixture of ethanol and 1× PBS at −20 °C.

Abiotic control

Abiotic controls of CH_4 formation were prepared using cell-free medium supplemented with 50 mM H_2O_2 and 5 µM $FeSO_4$ (and/or ferrihydrite) and incubated anaerobically in the dark at 35 °C for 24 h.

Cell counting

Cell counts were obtained using a Zeiss LSM 880 confocal microscope. From each culture, 50–200 µL of fixed sample (dependent on the growth stage) was diluted in 5 mL of 1× PBS and loaded onto a filter membrane (GTBP02500, Isopore, Merck Millipore, pore size: 0.22 µm). Cellular DNA was stained with Hoechst 33342 (1:10,000 (v/v) dilution in 1× PBS) for 10 min at room temperature, followed by three rinses in 1× PBS. 60–100 random fields of view (135 µm × 135 µm for each) on the membrane were imaged and analyzed using a custom MATLAB script. For ferrihydrite-amended cultures, Fe(III) minerals were dissolved using oxalate prior to processing[16].

The cell growth rate μ is defined as

$$\mu = \frac{d \ln N}{dt}, \tag{2}$$

whose numerical implementation followed a three-point central-difference formula for arbitrary function $y(x)$[65]

$$y_i' \approx \frac{y_{i+1} - \left(\frac{x_{i+1} - x_i}{x_i - x_{i-1}}\right)^2 y_{i-1} - \left[1 - \left(\frac{x_{i+1} - x_i}{x_i - x_{i-1}}\right)^2\right] y_i}{(x_{i+1} - x_i)\left(1 + \frac{x_{i+1} - x_i}{x_i - x_{i-1}}\right)}. \tag{3}$$

Here, x_i and y_i stand for t and $\ln N$ at the i-th time point, respectively.

Chemical analysis
CH_4 and CO_2 concentrations in the headspace were measured using a gas chromatograph (Shimadzu, GC-14B) equipped with a flame ionization detector and a packed column (Shimadzu, TDX-02, 2 m × 2 mm). Their soluble and total amounts were estimated using Henry's law. Since the pH of the solution was monitored to be stable at -7, the interconversion between CO_2, HCO_3^-, and CO_3^{2-} was neglected. Methylamines (monomethylamine, dimethylamine, trimethylamine) in the medium were converted to their volatile forms in sodium hydroxide solution (15 mM), and measured using a gas chromatograph (Shimadzu, GC-2010) equipped with a flame ionization detector and a capillary column (Agilent, CP-Volamine, 0.32 mm × 60 m). Results of the three methylamine species were integrated to estimate the total concentration of methyl in the culture as a function of time, known as the methyl concentration curve. Fe(II) concentration was determined using a microplate spectrophotometer (Hach, DR5000), employing the ferrozine method[64]. Soluble Fe(II) was measured directly from 0.5 mL of supernatant culture medium. Total Fe(II) was measured from 0.5 mL of culture medium after dissolving all its minerals using 2 M HCl[16]. Sulfide concentration was measured from 1 mL of supernatant culture medium using a microplate spectrophotometer (Hach, DR5000), employing the methylene blue method (Hach method 8131).

The consumption/production rate, r, of a given chemical species, is defined as

$$r = \frac{1}{N}\left|\frac{dC}{dt}\right|, \tag{4}$$

where N, C, and t denote cell number, chemical concentration, and time, respectively. The numerical implementation of this formula relied on Eq. (3).

Quantification of ROS
Cellular ROS levels were measured using a ROS assay kit (Beyotime, S0033M). Briefly, log-phase cultures (-25 hpi) under either optimal or ferrihydrite-amended conditions were anaerobically incubated with 10 μM 2′,7′-dichlorofluorescein diacetate (DCFH-DA) in the dark for 45 min at 37 °C. Following incubation, cells were harvested by centrifugation (4000 × g, 10 min) and washed three times with fresh culture medium (3 min each). The fluorescence of DCFH-DA in each sample was quantified using a microplate reader (Agilent BioTek Synergy H1) with an excitation wavelength of 488 nm and an emission wavelength of 525 nm. Fluorescence values were background-subtracted (using pure culture medium as the control) and normalized by cell number to determine the cellular ROS levels.

Stable carbon isotope measurement
Stable carbon isotope ratios were determined using an elemental analyzer-isotope ratio mass spectrometer (Elementar, Vario EL III-Isoprime). The headspace gas was fully combusted, and the resulting CO_2 was separated using a purge-and-trap adsorption column. The purified CO_2 was then passed to the isotope ratio mass spectrometer to measure the $^{13}C/^{12}C$ ratio. $\delta^{13}C$ values are expressed in the conventional δ notation in per mil versus Vienna Pee Dee Belemnite (VPDB), calculated as:

$$\delta^{13}C_{VPDB-Sample} = \left(\frac{(^{13}C/^{12}C)_{Sample}}{(^{13}C/^{12}C)_{Standard}}\right) - 1. \tag{5}$$

$\delta^{13}C$ values were corrected using a reference standard of high-purity L-glutamic acid (USGS40) with a $\delta^{13}C$ value of −26.39‰, calibrated against the International Atomic Energy Agency (IAEA) and National Institute of Standards and Technology (NIST) reference substances.

XRD measurement
30 mL of Fe(III)-amended cell culture was centrifuged (13,000 × g, 10 min), supernatant-removed, rinsed three times in double-distilled water, and freeze-dried to extract the solid component. Its mineral content was identified using a poly-functional X-ray diffractometer (XRD, D8 ADVANCE Da Vinci, Bruker) with Cu-Kα radiation setting in the 2θ range of 3° to 90° at an accuracy of 0.02°. The XRD Data were processed using Jade 6.5 software.

RT-qPCR
6 mL of each culture with intact cells was RNA-stabilized using RNAlater™ (Invitrogen, AM7024) and stored at −80 °C. Total RNA in the sample was extracted using PureLink RNA Mini Kit (Thermo Fisher, 12183018A) with on-column PureLink™ DNase (Thermo Fisher, 12185-010) treatment. RNA was converted to first-strand cDNA using SuperScript III first-strand synthesis system (Invitrogen, 18080-051) and stored at −20 °C. A plasmid with *mcrA* was used as a standard DNA[66]. *E. coli* DH5α containing the plasmid was cultured in LB medium with ampicillin (50 μg/mL) at 37 °C, 265 rpm, overnight (12 - 16 h). The plasmid was extracted from the culture using QIAprep Spin Miniprep Kit (QIAGEN, 27104).

RT-qPCR was performed on Applied Biosystems 7300 Real-Time PCR System (Thermo Fisher Scientific) using TB Green Premix Ex Taq II (TaKaRa, RR820A) and the following primers[66]: 5′-GGTGGTGTMGGDT TCACMCARTA-3′ and 5′-CGTTCATBGCGTAGTTVGGRTAGT-3′ (Sangon Biotech). Each reaction (20 μL) consisted of 10 μL of 2× TB Green Premix Ex Taq II, 0.4 μL of 50× ROX reference dye, 0.8 μL of 10 μM forward primer, 0.8 μL of 10 μM reverse primer, 1 μL of cDNA, and 7 μL of RNase-free water. Thermal cycles included a holding step of 5 min at 95 °C and 40 cycles of amplification (10 s at 95 °C followed by 30 s at 55 °C) and fluorescence collection (35 s at 72 °C). Tenfold dilutions of the plasmid DNA with *mcrA* were used for calibration. All reactions were carried out in triplicate.

smHCR-FISH probe design
Two sets of oligo-DNA probes were prepared for smHCR-FISH[31,32]: (1) a set of 61-nt primary probes, each with a 20-nt sequence complementary to the target mRNA, a 5-nt spacer, and a 36-nt HCR initiator to trigger amplification; (2) a set of two fluorophore-conjugated amplifier probes for labeling the initiator with HCR amplification. For each gene, primary probes were designed according to a previous protocol[23] (one probe for 16S rRNA, 6−9 probes for each other gene, Supplementary Table 1) and synthesized with HPLC purification (Sangon Biotech). Pre-designed amplifier probe sets, B2, B3, and B5[31] (Supplementary Table 1), were synthesized (Molecular Instruments) with fluorophore tags (Alexa Fluor™ 488 for B2 probes, Alexa Fluor™ 647 for B3 probes, and Alexa Fluor™ 555 for B5 probes).

Multi-round smHCR-FISH and imaging
A step-by-step protocol for multi-round smHCR-FISH and imaging has been deposited in the protocols.io repository[67]. Briefly, a 4-chamber glass-bottom dish (Cellvis, D35C4-20-1-N) was further divided into 12

wells using reagent barriers (FastWells, 70339-44) and bottom-coated with poly-L-Lysine (Sigma, P4707)[4]. Fixed cells from each time point were settled onto the bottom of a well for 2 h at room temperature. The dish was then mounted in the incubation system of a Zeiss LSM 880 laser scanning confocal microscope for multi-round smHCR-FISH.

For each round of the experiment, cells in each well were incubated in 40 μL of hybridization buffer (20 mM Tris-HCl, 25% (w/v) formamide, 250 mM EDTA, 2% (v/v) 50× Denhardt's solution, and 0.1% (v/v) Tween 20) with primary probes (0.1 μM for each gene) at 46 °C for 4 h. Following hybridization, cells were washed three times (20 min each) at 48 °C in 500 μL of wash buffer (159 mM NaCl, 20 mM Tris-HCl, 0.1% Tween 20). For HCR amplification, each amplifier probe was separately dissolved in amplification buffer (5× SSC, 10% dextran sulfate, 0.1% Tween 20, 150 nM probe), heated to 95 °C for 2 min, and cooled to room temperature for 30 min to open the hairpin structure. Cells were incubated with a 20-μL-mixture of all amplifier probes at 35 °C in a humid atmosphere for 1 h. After HCR amplification, cells were washed three times (10 min each) in 500 μL 4× SSC and stained with 1:10,000 diluted Hoechst 33342 (Invitrogen, H3570) for 10 min. Following three additional rinses in 4× SSC, cells were covered by a mixture of Aqua-poly/Mount (Polysciences, 18606) and 4× SSC (-3:10 (v/v)) for imaging.

Image acquisition was performed using a Zeiss LSM 880 laser scanning confocal microscope equipped with an Airyscan detector and a plan-Apochromat 63×/1.4 NA oil-immersion objective. 16-bit image stacks (15 z-slices for the optimal-growth-condition sample and 21 z-slices for the ferrihydrite-amended sample) were acquired with a pixel size of 0.035 μm and a z-step size of 0.16 μm. Fluorescence of Alexa Fluor™ 647, Alexa Fluor™ 555, Alexa Fluor™ 488, and Hoechst 33342 was excited using 633-nm, 561-nm, 488-nm, and 405-nm lasers, respectively. >200 cells in each well were imaged from 5–10 fields of view.

After imaging, HCR-FISH probes in the cell were removed using DNase I (TURBO™ DNase, AM2238)[32]. Briefly, cells in each well were washed in 50 μL of 1× DNase buffer for 5 min and incubated with 3 μL DNase I (2 Units/μL) in 1× DNase buffer at 37 °C for 2 h. Following enzyme digestion, cells were washed three times (10 min each) in wash buffer at 37 °C and fixed in 2% PFA for 15 min at room temperature to inactivate DNase I. After three more washes (10 min each) in 4× SSC, samples were ready for the next round of the experiment. From the second round on, since cellular DNA had been degraded in DNase I treatment, cellular RNA, instead of DNA, was stained for cell identification using POPO™-1 (Invitrogen, P3580).

In a separate experiment, pre-designed probes targeting a *Drosophila* gene (*hunchback*, Supplementary Table 1)[68], which is absent from the LMO-1 genome, were used as a negative control for our smHCR-FISH method. Applying these probes to LMO-1 resulted in near-zero signal of cellular fluorescence, with almost no fluorescent spots detected, significantly lower than those observed for LMO-1 genes (Supplementary Fig. 1), confirming the specificity of our method.

Image registration and cell segmentation

Image processing was performed using custom MATLAB scripts and ImageJ. Briefly, confocal data in Zeiss CZI format was converted to TIFF format. Maximum intensity projection (MIP) of cellular DNA (or RNA) signal was used to register images from each round of the experiment by MATLAB function "imregister". Automatic two-dimensional (2D) cell segmentation was performed on cellular DNA (or RNA) signal (MIP image for the optimal-growth-condition sample, brightest image layer for the ferrihydrite-amended sample) using the StarDist plugin of ImageJ[69]. Manual refinements and corrections of segmentation were done through ImageJ and custom MATLAB scripts. Since the ferrihydrite-amended sample typically contained multiple cell layers, the z-boundary of each segmented cell was determined as the 7th layer from the center layer of the brightest DNA or RNA signal.

mRNA quantification

Signal of each mRNA species was analyzed individually following a previously developed method[68,70]. Briefly, candidates for fluorescent spots were identified as 3D local maxima in the image stack, whose local intensity profiles were each fitted to a 2D Gaussian function to extract peak height (I_{peak}) and radius (σ_0). The intensity of each spot candidate was computed as $I = 2\pi I_{peak}\sigma_0^2$. By comparing the joint distribution of I_{peak} and σ_0 between the intracellular and extracellular spots, a 2D threshold was determined to distinguish real mRNA spots from background noise. The typical intensity, I_0, of a single mRNA molecule was determined by fitting the primary peak of the spot intensity distribution to a multi-Gaussian function (Fig. 1d). Compared to other methods that pooled data from multiple mRNA species together to determine a common I_0[4], our individual estimation of I_0 for each mRNA species ensures more accurate quantification of every gene's expression. mRNA copy number within a cell was estimated by dividing the total intensity of fluorescent spots inside the cell by I_0. For further analysis of gene expression, we excluded cells lost during DNase I treatment, expressing only one type of mRNA, or with mRNA levels in the highest 2%.

Ribosome level quantification

Cellular ribosome levels were quantified based on the ribosome FISH signal. Briefly speaking, for each cell, we computed the total FISH signal within the cell mask on each z layer. The maximum fluorescence among all layers were used to represent the ribosome level of the cell. Signals from different cells (pooling all time points together) were normalized to the brightest cell before further analysis.

Quantification of *katG* (catalase/peroxidase HPI) expression

katG mRNA was labeled, imaged, and quantified in a single-round smHCR-FISH experiment following the same protocol.

Dimensionality reduction and cluster analysis of single-cell gene expression

Single-cell UMAP analysis was performed using Scanpy v1.9.5[49], following standard procedures for normalization, scaling, dimensionality reduction, and clustering, as described in the Scanpy tutorial, excluding a library size normalization. For both optimal and ferrihydrite-amended conditions, the analysis incorporated 15 neighbors and 11 principal component analysis (PCA) components. Clustering was conducted using the Leiden method. Clusters in two growth conditions were aligned using the "ingest" function, with data from the optimal growth condition serving as the annotated reference.

Mathematical modeling of transcriptional kinetics

Model description. We employed a regular two-state model to describe the stochastic transcriptional kinetics of archaeal genes[50]. The model assumes that the gene randomly switches between two transcription states: an "OFF" state (denoted as state 0), where the gene is transcriptionally inactive, and an "ON" state (denoted as state 1), where the gene is transcriptionally active. mRNA synthesis only occurs in the "ON" state. State transitions from "OFF" to "ON" and from "ON" to "OFF", and mRNA synthesis are all assumed to follow Poisson processes with gene activation rate k_{01} (or k_{ON}), gene inactivation rate k_{10} (or k_{OFF}), and mRNA production rate k_{TX}, respectively. After being produced, each mRNA molecule degrades randomly with a Poissonian rate k_D. Since DNA replicates during the cell cycle (Fig. 1f), we introduced a parameter α to denote the fraction of cells with two gene copies. Additionally, to account for the finite labeling efficiency of smFISH, we defined a parameter p_0 to denote the fraction of unlabeled cells.

Note that we omitted modeling the detailed process of nascent mRNA synthesis (e.g., elongation). This omission is justified because the half-life of mRNA in a methanogen was shown to be about 10% of

the cell cycle[71], i.e., ~30 min for LMO-1, much longer than the time scale of mRNA synthesis (~1 min). Moreover, since the mRNA lifetime is much shorter than the cell cycle, the observed mRNA copy number distribution may be approximated to be in a quasi-steady state.

Master equation. The state of a cell with one gene copy is described by the gene state n ($n = 0, 1$) and the mRNA copy number m ($m = 0, 1, 2, ...$), whose probability distribution $P(n,m)$ follows a master equation:

$$\begin{cases} \dot{P}(0,m) = -k_{ON}P(0,m) + k_{OFF}P(1,m) - mk_DP(0,m) + (m+1)k_DP(0,m+1) \\ \dot{P}(1,m) = k_{ON}P(0,m) - k_{OFF}P(1,m) - mk_DP(1,m) + (m+1)k_DP(1,m+1) \\ \qquad - k_{TX}P(1,m) + k_{TX}P(1,m-1) \end{cases} \tag{6}$$

The equation may be rewritten in a matrix form:

$$\dot{\mathbf{P}} = \mathbf{QP} = \begin{bmatrix} \mathbf{K-T} & \mathbf{D} & 0 & 0 & \cdots \\ \mathbf{T} & \mathbf{K-T-D} & 2\mathbf{D} & 0 & \cdots \\ 0 & \mathbf{T} & \mathbf{K-T-2D} & 3\mathbf{D} & \cdots \\ 0 & 0 & \mathbf{T} & \mathbf{K-T-3D} & \cdots \\ \vdots & \vdots & \vdots & \vdots & \ddots \end{bmatrix} \begin{bmatrix} \mathbf{P}_0 \\ \mathbf{P}_1 \\ \mathbf{P}_2 \\ \mathbf{P}_3 \\ \vdots \end{bmatrix}, \tag{7}$$

where $\mathbf{P} = \begin{bmatrix} \mathbf{P}_0 \\ \mathbf{P}_1 \\ \mathbf{P}_2 \\ \vdots \end{bmatrix} = \begin{bmatrix} \begin{bmatrix} P(0,0) \\ P(1,0) \end{bmatrix} \\ \begin{bmatrix} P(0,1) \\ P(1,1) \end{bmatrix} \\ \begin{bmatrix} P(0,2) \\ P(1,2) \end{bmatrix} \\ \vdots \end{bmatrix}$ is the probability matrix, while

$\mathbf{K} = \begin{bmatrix} -k_{ON} & k_{OFF} \\ k_{ON} & -k_{OFF} \end{bmatrix}$, $\mathbf{T} = \begin{bmatrix} 0 & 0 \\ 0 & k_{TX} \end{bmatrix}$, and $\mathbf{D} = \begin{bmatrix} k_D & 0 \\ 0 & k_D \end{bmatrix}$ are matrices describing gene-state transitions, mRNA synthesis, and degradation, respectively.

With steady-state approximation, Eq. (7) is simplified into a linear algebraic equation

$$\begin{bmatrix} \mathbf{K-T} & \mathbf{D} & 0 & 0 & \cdots \\ \mathbf{T} & \mathbf{K-T-D} & 2\mathbf{D} & 0 & \cdots \\ 0 & \mathbf{T} & \mathbf{K-T-2D} & 3\mathbf{D} & \cdots \\ 0 & 0 & \mathbf{T} & \mathbf{K-T-3D} & \cdots \\ \vdots & \vdots & \vdots & \vdots & \ddots \end{bmatrix} \begin{bmatrix} \mathbf{P}_0 \\ \mathbf{P}_1 \\ \mathbf{P}_2 \\ \mathbf{P}_3 \\ \vdots \end{bmatrix} = 0. \tag{8}$$

Note that Eq. (8) only depends on ratios k_{ON}/k_D, k_{OFF}/k_D, and k_{TX}/k_D, effectively removing k_D as an independent parameter. In this paper, we set k_D to be constant based on the previous study of archaeal mRNA lifetime[71].

Numerically solving the master equation. Equation (8) involves an infinite number of equations for varying m. While the analytical solution is feasible[50], numerical methods offer greater convenience and adaptability for inference. In this paper, we adopted the finite state projection (FSP) method for numerical solution[50,70]. Briefly, using a finite range of m ($0 \le m \le 80$) to cover the main portion of the observed distribution, we truncated Eq. (8) into a finite-dimensional form, which enables straightforward solution.

Correction for DNA replication and finite labeling efficiency. For cells with two gene copies, we assumed independent expression from each gene copy[24,68]. Further considering the finite efficiency of FISH labeling, we wrote the observed mRNA copy number distribution for a

mixture of cells with/without DNA replication as

$$P_{ob}(m) = (1 - p_0)[(1 - \alpha)P(m) + \alpha P(m)*P(m)] + p_0\delta_{m,0}, \tag{9}$$

where "$*$" represents convolution. In this paper, we experimentally determined α from the DNA signal of the cell (Fig. 1f).

Inferring the transcription kinetics. We applied the maximum likelihood estimation (MLE) method to infer the kinetic parameters of each gene from the experimental data[24,70]. Briefly, for a given set of parameters $\mathbf{K} = \{k_{ON}, k_{OFF}, k_{TX}, p_0\}$, the probability of observing m mRNAs in a cell is $P(m | \mathbf{K})$. Thus, the likelihood of $\mathbf{K}$ for a given dataset $\mathbf{M} = \{m_1, m_2, ...\}$ is

$$L(\mathbf{M} | \mathbf{K}) = \prod_j P(m_j | \mathbf{K}). \tag{10}$$

For data from each time point, we optimized the fit by maximizing L (or log$L$) across a broad range of parameter values (k_{ON}/k_D: 0.01–10, k_{OFF}/k_D: 0.01–50, k_{TX}/k_D: 0–110, p_0: 0–1) using a combination of simplex and simulated annealing methods.

Comparing parameters extracted from different time points revealed that k_{ON} and k_{OFF} were key variables in the regulation, while k_{TX} stayed stable (Supplementary Fig. 10a). Therefore, we refined the fitting by assuming that only k_{ON} and k_{OFF} vary with time.

Cluster analysis of kinetic parameters
For either k_{ON} or k_{OFF}, we performed k-means clustering on the log-phase data for all genes using the MATLAB function "kmeans" with 100 replicates to ensure stable outcomes. The first two time points in ferrihydrite amendment data were excluded to omit the methyl-radical-induced initial spike. For each cluster, we determined a characteristic temporal pattern by averaging all corresponding raw data. To further relate k_{ON} and k_{OFF} clusters, we computed the Pearson correlation coefficient among their characteristic patterns and applied a threshold ($r = 0.9$) to discern correlated clusters (Supplementary Fig. 10b–e).

Statistics and reproducibility
All bulk measurements were conducted with three biological replicates (independent cultures). Most smHCR-FISH measurements (except the comparisons with RT-qPCR) of log-phase time points were performed with two biological replicates, while those for the inactive lag- and stationary-phase time points were performed with one biological replicate. For optimal growth condition, a total of 102,145 cells across 12 time points were imaged, with ≥2568 cells captured from ≥2 randomly allocated FOVs at each time point. For ferrihydrite-amended condition, a total of 32,296 cells across 10 time points were imaged, with ≥255 cells captured from ≥2 randomly allocated FOVs at each time point. These sample sizes are comparable to those reported in previous publications[4,72,73], sufficient for single-cell statistical analyses. Comparisons between smHCR-FISH and RT-qPCR were conducted with three biological replicates. Each RT-qPCR measurement was performed with three technical replicates, while all other experiments were conducted without technical replication.

The sample sizes for each smHCR-FISH plot are listed as follows: Fig. 1e: time points from early to late, $n = 3666, 6742, 6375, 7118, 6476, 4329$, and 3909 cells. Figure 2e, f: time points from early to late, $n = 8787, 15,150, 14,001, 15,835, 23,096, 4707, 5346, 2568, 3575, 3017, 3009$, and 3054 cells. Figure 3f: $n = 3879$ and 1412 cells for optimal and ferrihydrite-amended conditions, respectively. Figure 3h, i: time points from early to late, $n = 953, 3953, 7205, 7219, 9794, 255, 468, 1545, 953$, and 904 cells. Figure 4: $n = 32,885$ and 6408 cells for optimal and ferrihydrite-amended conditions, respectively. Figure 5: time points from early to late, $n = 1357, 625, 2862, 2765, 4707, 5346, 2568, 3575, 3017, 3009$, and 3054 cells for optimal condition; $n = 315, 304, 678, 986, 255, 468, 1545, 953$, and 904 cells for ferrihydrite-amended

condition. Supplementary Fig. 1c: $n = 2052$ and 1271 cells for negative and positive samples, respectively. Supplementary Fig. 2: time points from early to late, $n = 1524$, 698, 3226, 3143, 5333, 6071, 3028, 4289, and 3523 cells. Supplementary Fig. 3: time points from early to late, $n = 15{,}150$, 14,001, 15,835, and 23,096 cells. Supplementary Fig. 4a, b: time points from early to late, $n = 349$, 341, 777, 1117, 289, 532, and 1755 cells. Supplementary Fig. 5a, b: time points from early to late, $n = 3953$, 7205, 7219, and 9794 cells. Supplementary Fig. 5c: $n \geq 105$ biofilm-forming cells and ≥ 566 planktonic cells. Supplementary Figs. 6, 7: $n = 32{,}885$ and 6408 cells for optimal and ferrihydrite-amended conditions, respectively. Supplementary Figs. 8–10: time points from early to late, 1357, 625, 2862, 2765, 4707, 5346, 2568, 3575, 3017, 3009, and 3054 cells for optimal condition; $n = 315$, 304, 678, 986, 255, 468, 1545, 953, and 904 cells for ferrihydrite-amended condition.

It is worth noting that the error bars in Figs. 2e, f, 3f, h, i were estimated by comparing data across FOVs. These gene expression differences between FOVs primarily reflect cell-to-cell heterogeneity in gene expression rather than technical noise. Such heterogeneity arises from the inherent stochasticity of biochemical reactions[3,52] and non-uniform micro-environments within the sample[4], both of which contribute to variations between biological replicates. Including these between-FOV differences in error bar computations serves as a supplementary measure when biological replicates are limited. However, we emphasize that such statistical analysis cannot replace the investigation of biological replicates.

Reporting summary
Further information on research design is available in the Nature Portfolio Reporting Summary linked to this article.

Data availability
The raw image data reported in this paper are available in a private server under accession code http://gofile.me/4yuzx/zbFlbhcpr. A smaller representative image dataset has been deposited in the Zenodo database under accession code https://doi.org/10.5281/zenodo.14684947[74]. Source data are provided with this paper.

Code availability
The custom MATLAB scripts for data analysis and mathematical modeling are available at https://github.com/Xulab-biophysics/smHCR-FISH2024 and https://doi.org/10.5281/zenodo.14684947[74].

References

1. Bennett, M. R. et al. Metabolic gene regulation in a dynamically changing environment. *Nature* **454**, 1119–1122 (2008).
2. Carthew, R. W. Gene regulation and cellular metabolism: an essential partnership. *Trends Genet.* **37**, 389–400 (2021).
3. Raj, A. & van Oudenaarden, A. Nature, nurture, or chance: stochastic gene expression and its consequences. *Cell* **135**, 216–226 (2008).
4. Dar, D., Dar, N., Cai, L. & Newman, D. K. Spatial transcriptomics of planktonic and sessile bacterial populations at single-cell resolution. *Science* **373**, eabi488 (2021).
5. Ackermann, M. A functional perspective on phenotypic heterogeneity in microorganisms. *Nat. Rev. Microbiol.* **13**, 497–508 (2015).
6. Baker, B. J. et al. Diversity, ecology and evolution of Archaea. *Nat. Microbiol.* **5**, 887–900 (2020).
7. Hatzenpichler, R., Krukenberg, V., Spietz, R. L. & Jay, Z. J. Next-generation physiology approaches to study microbiome function at single cell level. *Nat. Rev. Microbiol.* **18**, 241–256 (2020).
8. Kaster, A. K. & Sobol, M. S. Microbial single-cell omics: the crux of the matter. *Appl. Microbiol. Biotechnol.* **104**, 8209–8220 (2020).
9. Evans, P. N. et al. An evolving view of methane metabolism in the Archaea. *Nat. Rev. Microbiol.* **17**, 219–232 (2019).
10. Welte, C. & Deppenmeier, U. Bioenergetics and anaerobic respiratory chains of aceticlastic methanogens. *Biochim. Biophys. Acta* **1837**, 1130–1147 (2014).
11. Sauterey, B., Charnay, B., Affholder, A., Mazevet, S. & Ferrière, R. Co-evolution of primitive methane-cycling ecosystems and early Earth's atmosphere and climate. *Nat. Commun.* **11**, 2705 (2020).
12. Shalvarjian, K. E. & Nayak, D. D. Transcriptional regulation of methanogenic metabolism in archaea. *Curr. Opin. Microbiol.* **60**, 8–15 (2021).
13. Yoon, S. H. et al. A systems level predictive model for global gene regulation of methanogenesis in a hydrogenotrophic methanogen. *Genome Res.* **23**, 1839–1851 (2013).
14. Zhuang, L., Xu, J., Tang, J. & Zhou, S. Effect of ferrihydrite biomineralization on methanogenesis in an anaerobic incubation from paddy soil. *J. Geophys. Res. Biogeosci.* **120**, 876–886 (2015).
15. D'Hondt, S. et al. Distributions of microbial activities in deep subseafloor sediments. *Science* **306**, 2216–2221 (2004).
16. Prakash, D., Chauhan, S. S. & Ferry, J. G. Life on the thermodynamic edge: respiratory growth of an acetotrophic methanogen. *Sci. Adv.* **5**, eaaw9059 (2019).
17. Yamada, C., Kato, S., Kimura, S., Ishii, M. & Igarashi, Y. Reduction of Fe(III) oxides by phylogenetically and physiologically diverse thermophilic methanogens. *FEMS Microbiol. Ecol.* **89**, 637–645 (2014).
18. Bodegom, P. M., Scholten, J. C. & Stams, A. J. Direct inhibition of methanogenesis by ferric iron. *FEMS Microbiol. Ecol.* **49**, 261–268 (2004).
19. Xu, L. et al. Methyl-compounds driven benthic carbon cycling in the sulfate-reducing sediments of South China Sea. *Environ. Microbiol.* **23**, 641–651 (2021).
20. Schorn, S. et al. Diverse methylotrophic methanogenic archaea cause high methane emissions from seagrass meadows. *Proc. Natl. Acad. Sci. USA* **119**, 2106628119 (2022).
21. Xiao, K.-Q., Moore, O. W., Babakhani, P., Curti, L. & Peacock, C. L. Mineralogical control on methylotrophic methanogenesis and implications for cryptic methane cycling in marine surface sediment. *Nat. Commun.* **13**, 2722 (2022).
22. Moffitt, J. R., Lundberg, E. & Heyn, H. The emerging landscape of spatial profiling technologies. *Nat. Rev. Genet.* **23**, 741–759 (2022).
23. Raj, A., van den Bogaard, P., Rifkin, S. A., van Oudenaarden, A. & Tyagi, S. Imaging individual mRNA molecules using multiple singly labeled probes. *Nat. Methods* **5**, 877–879 (2008).
24. Wang, M., Zhang, J., Xu, H. & Golding, I. Measuring transcription at a single gene copy reveals hidden drivers of bacterial individuality. *Nat. Microbiol.* **4**, 2118–2127 (2019).
25. Zoller, B., Little, S. C. & Gregor, T. Diverse spatial expression patterns emerge from unified kinetics of transcriptional bursting. *Cell* **175**, 835–847.e825 (2018).
26. Wagner, M., Horn, M. & Daims, H. Fluorescence in situ hybridization for the identification and characterisation of prokaryotes. *Curr. Opin. Microbiol.* **6**, 302–309 (2003).
27. van Wolferen, M., Pulschen, A. A., Baum, B., Gribaldo, S. & Albers, S.-V. The cell biology of archaea. *Nat. Microbiol.* **7**, 1744–1755 (2022).
28. Kawakami, S. et al. Detection of single-copy functional genes in prokaryotic cells by two-pass TSA-FISH with polynucleotide probes. *J. Microbiol. Methods* **88**, 218–223 (2012).
29. Harris, R. L. et al. FISH-TAMB, a fixation-free mRNA fluorescent labeling technique to target transcriptionally active members in microbial communities. *Microb. Ecol.* **84**, 182–197 (2021).
30. Yamaguchi, T. et al. Rapid and sensitive identification of marine bacteria by an improved in situ DNA hybridization chain reaction (quickHCR-FISH). *Syst. Appl. Microbiol.* **38**, 400–405 (2015).
31. Choi, H. M. T. et al. Mapping a multiplexed zoo of mRNA expression. *Development* **143**, 3632–3637 (2016).

32. Shah, S., Lubeck, E., Zhou, W. & Cai, L. In situ transcription profiling of single cells reveals spatial organization of cells in the mouse hippocampus. *Neuron* **92**, 342–357 (2016).

33. Liang, L. et al. *Methanococcoides orientis* sp. nov., a methylotrophic methanogen isolated from sediment of the East China Sea. *Int. J. Syst. Evol. Microbiol.* **72**, 005384 (2022).

34. Morono, Y., Kubota, K., Tsukagoshi, D. & Terada, T. EDTA-FISH: a simple and effective approach to reduce non-specific adsorption of probes in fluorescence in situ hybridization (FISH) for environmental samples. *Microbes Environ.* **35**, ME20062 (2020).

35. Skinner, S. O., Sepúlveda, L. A., Xu, H. & Golding, I. Measuring mRNA copy number in individual *Escherichia coli* cells using single-molecule fluorescent in situ hybridization. *Nat. Protoc.* **8**, 1100–1113 (2013).

36. Chen, H., Shiroguchi, K., Ge, H. & Xie, X. S. Genome-wide study of mRNA degradation and transcript elongation in *Escherichia coli*. *Mol. Syst. Biol.* **11**, 808 (2015).

37. French, S. L., Santangelo, T. J., Beyer, A. L. & Reeve, J. N. Transcription and translation are coupled in Archaea. *Mol. Biol. Evol.* **24**, 893–895 (2007).

38. Matamouros, S. et al. Growth-rate dependency of ribosome abundance and translation elongation rate in *Corynebacterium glutamicum* differs from that in *Escherichia coli*. *Nat. Commun.* **14**, 5611 (2023).

39. Alon, U. *An Introduction to Systems Biology: Design Principles of Biological Circuits*, Ch. 5 (Chapman & Hall/CRC Press, 2007).

40. Gupta, D., Chen, K., Elliott, S. J. & Nayak, D. D. MmcA is an electron conduit that facilitates both intracellular and extracellular electron transport in *Methanosarcina acetivorans*. *Nat. Commun.* **15**, 3300 (2024).

41. Vijay, S. et al. Mycobacterial cultures contain cell size and density specific sub-populations of cells with significant differential susceptibility to antibiotics, oxidative and nitrite stress. *Front. Microbiol.* **8**, 463 (2017).

42. Smethurst, D. G. J., Kovalev, N., McKenzie, E. R., Pestov, D. G. & Shcherbik, N. Iron-mediated degradation of ribosomes under oxidative stress is attenuated by manganese. *J. Biol. Chem.* **295**, 17200–17214 (2020).

43. Stewart, P. S. & Franklin, M. J. Physiological heterogeneity in biofilms. *Nat. Rev. Microbiol.* **6**, 199–210 (2008).

44. Liu, J. et al. Metabolic co-dependence gives rise to collective oscillations within biofilms. *Nature* **523**, 550–554 (2015).

45. Ernst, L. et al. Methane formation driven by reactive oxygen species across all living organisms. *Nature* **603**, 482–487 (2022).

46. Wongnate, T. et al. The radical mechanism of biological methane synthesis by methyl-coenzyme M reductase. *Science* **352**, 953–958 (2016).

47. Ernst, L. et al. Methane formation driven by light and heat prior to the origin of life and beyond. *Nat. Commun.* **14**, 4364 (2023).

48. Wagner, T., Koch, J., Ermler, U. & Shima, S. Methanogenic heterodisulfide reductase (HdrABC-MvhAGD) uses two noncubane [4Fe-4S] clusters for reduction. *Science* **357**, 699–703 (2017).

49. Wolf, F. A., Angerer, P. & Theis, F. J. SCANPY: large-scale single-cell gene expression data analysis. *Genome Biol.* **19**, 15 (2018).

50. So, L.-H. et al. General properties of transcriptional time series in *Escherichia coli*. *Nat. Genet.* **43**, 554–560 (2011).

51. Munsky, B., Neuert, G. & van Oudenaarden, A. Using gene expression noise to understand gene regulation. *Science* **336**, 183–187 (2012).

52. Sanchez, A. & Golding, I. Genetic determinants and cellular constraints in noisy gene expression. *Science* **342**, 1188–1193 (2013).

53. Stark, R., Grzelak, M. & Hadfield, J. RNA sequencing: the teenage years. *Nat. Rev. Genet.* **20**, 631–656 (2019).

54. Ding, J., Sharon, N. & Bar-Joseph, Z. Temporal modelling using single-cell transcriptomics. *Nat. Rev. Genet.* **23**, 355–368 (2022).

55. Jovanovic, M. et al. Immunogenetics. Dynamic profiling of the protein life cycle in response to pathogens. *Science* **347**, 1259038 (2015).

56. Eden, E. et al. Proteome half-life dynamics in living human cells. *Science* **331**, 764–768 (2011).

57. Lyu, Z. & Lu, Y. Metabolic shift at the class level sheds light on adaptation of methanogens to oxidative environments. *ISME J.* **12**, 411–423 (2018).

58. Blombach, F., Matelska, D., Fouqueau, T., Cackett, G. & Werner, F. Key concepts and challenges in archaeal transcription. *J. Mol. Biol.* **431**, 4184–4201 (2019).

59. Martinez-Pastor, M., Tonner, P. D., Darnell, C. L. & Schmid, A. K. Transcriptional regulation in Archaea: from individual genes to global regulatory networks. *Annu. Rev. Genet.* **51**, 143–170 (2017).

60. Weidemüller, P., Kholmatov, M., Petsalaki, E. & Zaugg, J. B. Transcription factors: bridge between cell signaling and gene regulation. *Proteomics* **21**, e2000034 (2021).

61. McGlynn, S. E., Chadwick, G. L., Kempes, C. P. & Orphan, V. J. Single cell activity reveals direct electron transfer in methanotrophic consortia. *Nature* **526**, 531–535 (2015).

62. Tao, Y. et al. Highly efficient and robust π-FISH rainbow for multiplexed in situ detection of diverse biomolecules. *Nat. Commun.* **14**, 443 (2023).

63. Bourceau, P. et al. Visualization of metabolites and microbes at high spatial resolution using MALDI mass spectrometry imaging and in situ fluorescence labeling. *Nat. Protoc.* **18**, 3050–3079 (2023).

64. Liang, L. et al. Iron (oxyhydr)oxides shift the methanogenic community in deep sea methanic sediment—insights from long-term high-pressure incubations. *Sci. Total Environ.* **848**, 157590 (2022).

65. Sundqvist, H. & Veronis, G. A simple finite-difference grid with non-constant intervals. *Tellus* **22**, 26–31 (1970).

66. Niu, M., Fan, X., Zhuang, G., Liang, Q. & Wang, F. Methane-metabolizing microbial communities in sediments of the Haima cold seep area, northwest slope of the South China Sea. *FEMS Microbiol. Ecol.* **93**, fix101 (2017).

67. Dong, Y., Qi, L., Wang, F. & Xu, H. Multi-round smHCR-FISH for archaea. https://doi.org/10.17504/protocols.io.bp2l6dpm1vqe/v1 (2025).

68. Wang, J., Zhang, S., Lu, H. & Xu, H. Differential regulation of alternative promoters emerges from unified kinetics of enhancer-promoter interaction. *Nat. Commun.* **13**, 2714 (2022).

69. Schmidt, U., Weigert, M., Broaddus, C. & Myers, G. Cell detection with star-convex polygons. In *Proc. International Conference on Medical Image Computing and Computer-assisted Intervention*, 265–273 (Springer, 2018).

70. Xu, H., Sepúlveda, L. A., Figard, L., Sokac, A. M. & Golding, I. Combining protein and mRNA quantification to decipher transcriptional regulation. *Nat. Methods* **12**, 739–742 (2015).

71. Peterson, J. R. et al. Genome-wide gene expression and RNA half-life measurements allow predictions of regulation and metabolic behavior in *Methanosarcina acetivorans*. *BMC Genomics* **17**, 924 (2016).

72. Fang, R. et al. Conservation and divergence of cortical cell organization in human and mouse revealed by MERFISH. *Science* **377**, 56–62 (2022).

73. Takei, Y. et al. Integrated spatial genomics reveals global architecture of single nuclei. *Nature* **590**, 344–350 (2021).

74. Dong, Y. et al. Uncovering dynamic transcriptional regulation of methanogenesis via single-cell imaging of archaeal gene expression. Zenodo https://doi.org/10.5281/zenodo.14684947 (2025).

Acknowledgements

Author contributions

Conceptualization by Y.D., F.W., and H.X.; Methodology by Y.D., L.Q., Y.C., L.L., F.W., and H.X.; Software by Y.D., L.Q., F.Z., and H.X.; Formal Analysis by Y.D., and H.X.; Investigation by Y.D., J.W., W.Z., F.W., and H.X.; Writing—Original Draft by Y.D., F.Z., F.W., and H.X.; Writing—Revised Draft by Y.D., F.W., and H.X.; Funding acquisition by L.L., F.W. and H.X.; Resources by F.W. and H.X.; and Supervision by F.W. and H.X.

Competing interests

The authors declare no competing interests.

Additional information

Supplementary information The online version contains supplementary material available at
https://doi.org/10.1038/s41467-025-57159-0.

Correspondence and requests for materials should be addressed to Fengping Wang or Heng Xu.

Peer review information *Nature Communications* thanks Ranjani Murali and the other anonymous reviewers for their contribution to the peer review of this work. A peer review file is available.

Reprints and permissions information is available at
http://www.nature.com/reprints

Publisher's note Springer Nature remains neutral with regard to jurisdictional claims in published maps and institutional affiliations.